CHAPTER 5

AVO Modeling

5.1 Angle Stack Generation

The Elastic Impedance (EI) is an operation of P-wave velocity, S-wave velocity, density and incident angle. Therefore, to perform Elastic Impedance inversion, it is necessary to generate stacked data in angle domain instead of conventional offset domain. The angle ranges used for EI inversion and AVO modeling in this study are near (from 0 degree to 13 degrees), middle (from 13 degrees to 26 degrees) and far (from 26 to 40 degrees) angle stacks. The angle stacks are created through two steps, the first step is performing the angle gathers with appropriate incident angles and the second step is stacking the angle gathers to generate the angle stacks.

The angle gather process transform the input CPD gathers from the offset domain to incident angle domain using the defined velocity field. The velocity field is defined using root mean square (RMS) velocity in seismic processing as shown in chapter 3 (Figure 3.22). From Figure 3.22, because the largest incident angle at zone of interest is defined about 40 degrees, the incident angle range for near angle gathers is from 0 degree to 13 degrees, for middle angle gathers is from 13 degrees to 26 degrees and for far angle gathers is from 26 degrees to 40 degrees (Figure 5.1).

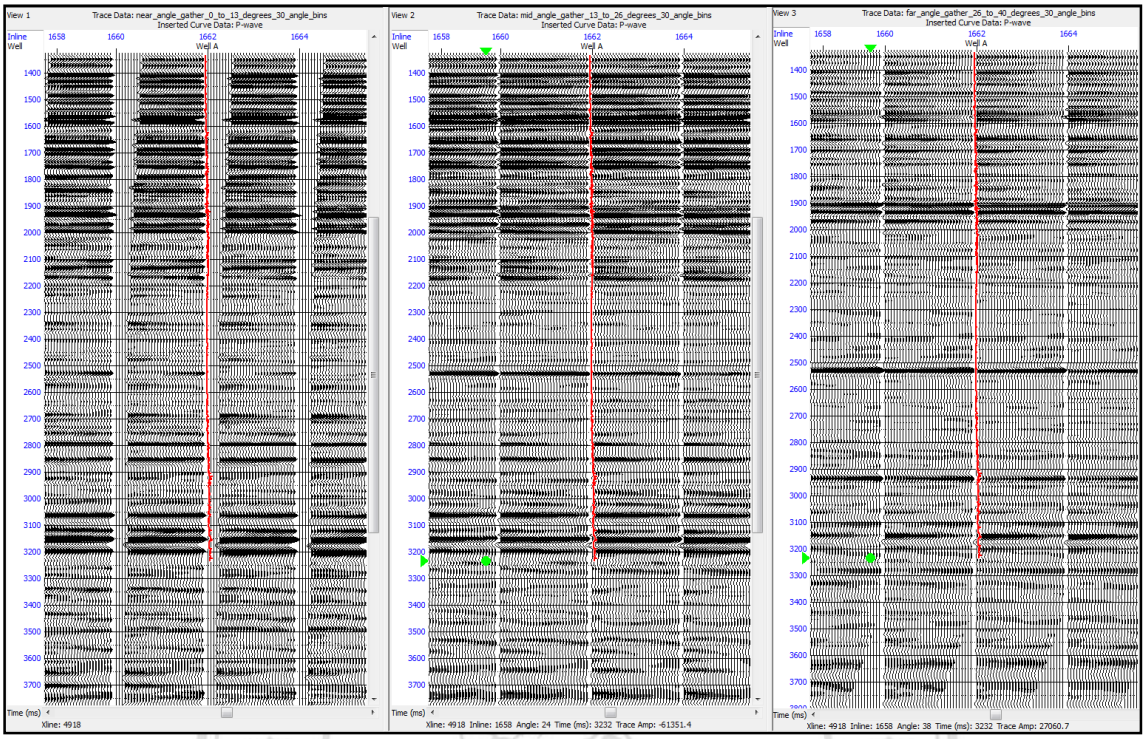

Figure 5.1: Near, mid and far angle gathers (from left to right) at the Well A location.

After generating the near, mid and far angle gathers, stacking function in Hampson Russell software is used for generating near, mid and far angle stacks. Stacking process will stack all traces in each gathers that fall within the range limits and the resulting traces will be displayed in a new volume. The near, mid and far angle stacked volumes are shown in Figure 5.2. The variations of reflection amplitude are seen clearly between near, mid and far angle stacks.

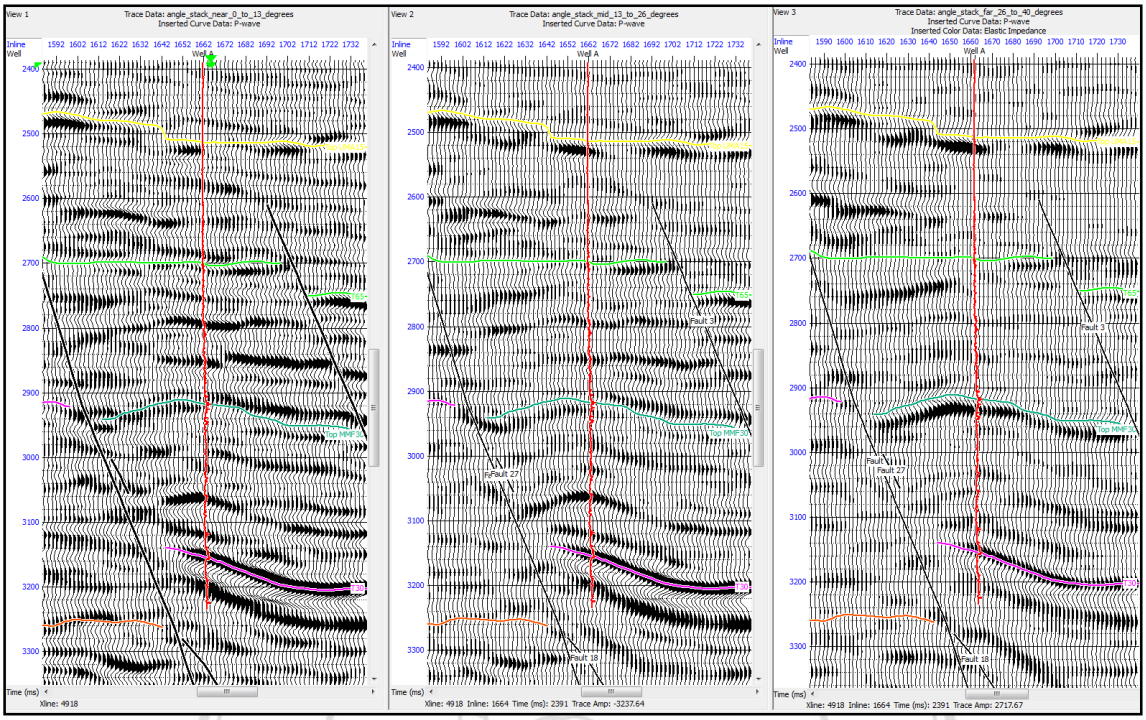

Figure 5.2: Near, mid and far angle stacked volumes (from left to right) at the Well A location with picked horizons.

5.2 Well to Seismic Tie

Well ties are a very important part of seismic interpretation. Well to seismic ties process is to conduct an experiment to test the connection between the geology and the seismic data (Simm and Bacon, 2014). The well to seismic ties process provides a means of correctly identifying horizons to pick, and estimating the wavelet for inverting seismic data to impedance (White and Simm, 2003). The procedure for tying well logs synthetic seismogram to seismic data in this study followed the procedure outlined by White and Simm (2003), as following steps in order:

- Edit and calibrate the sonic and density logs with checkshot data.
- Construct the synthetic seismogram from the input calibrated sonic and density logs. This step including choosing the appropriate reflection series (usually primaries only) and constructing the reflection series in two-way time.
- Perform the match, including determination the best match location and estimation the wavelet and its accuracy.

The first step is mentioned in chapter 4 above in the time – depth conversion part while two next steps are discussed in this chapter.

The well ties are carried out for both full stack and near, mid and far angle stacks volumes. Before wavelet estimation, correlating the well needs to be handled. The process of correlating the well is included extract a wavelet, correlate the well and compare with the resulting synthetic as shown in Figure 5.3. There are two basic methods for extracting the wavelet. One method uses the well and seismic data that can give a good estimate of both amplitude and phase spectra of the wavelet. However, that method cannot be used until the well is correlated. Another method uses just seismic data and the wavelet that is extracted from seismic data alone called statistical wavelet. This method just provides information about the amplitude spectrum of the wavelet and we must assume the phase of the wavelet is zero phase. In this study, both two methods are used to correlate the well.

As mentioned above, the horizons are identified using formation tops in the Well A after well to seismic matching in the full stack volume. And the wavelet estimated from the full stack volume is used for generating AVO synthetics models for the reservoirs. Meanwhile, the wavelets estimated from each angle stacks volumes are used for impedance inversion. Wavelet estimation is very important in seismic inversion and AVO analysis because it will be used to convolve with the reflection series of well or seismic data to produce the synthetic seismograms and to be removed from seismic volume to achieve the reflection coefficients in reflectivity inversion process. There are number of approaches to estimating the wavelet that mentioned by White and Simm (2003) like forward modeling approach, phase rotation of zero phase synthetic and wavelet estimation through matching. In this study, the way to extract the wavelet of seismic data is the phase rotation of zero phase synthetic approach as shown in Figure 5.3. The reason why this method is useful is because after processing, the phase of the seismic wavelet is usually linear across the seismic bandwidth. The goal of wavelet estimation is to achieve the original wavelet of seismic data.

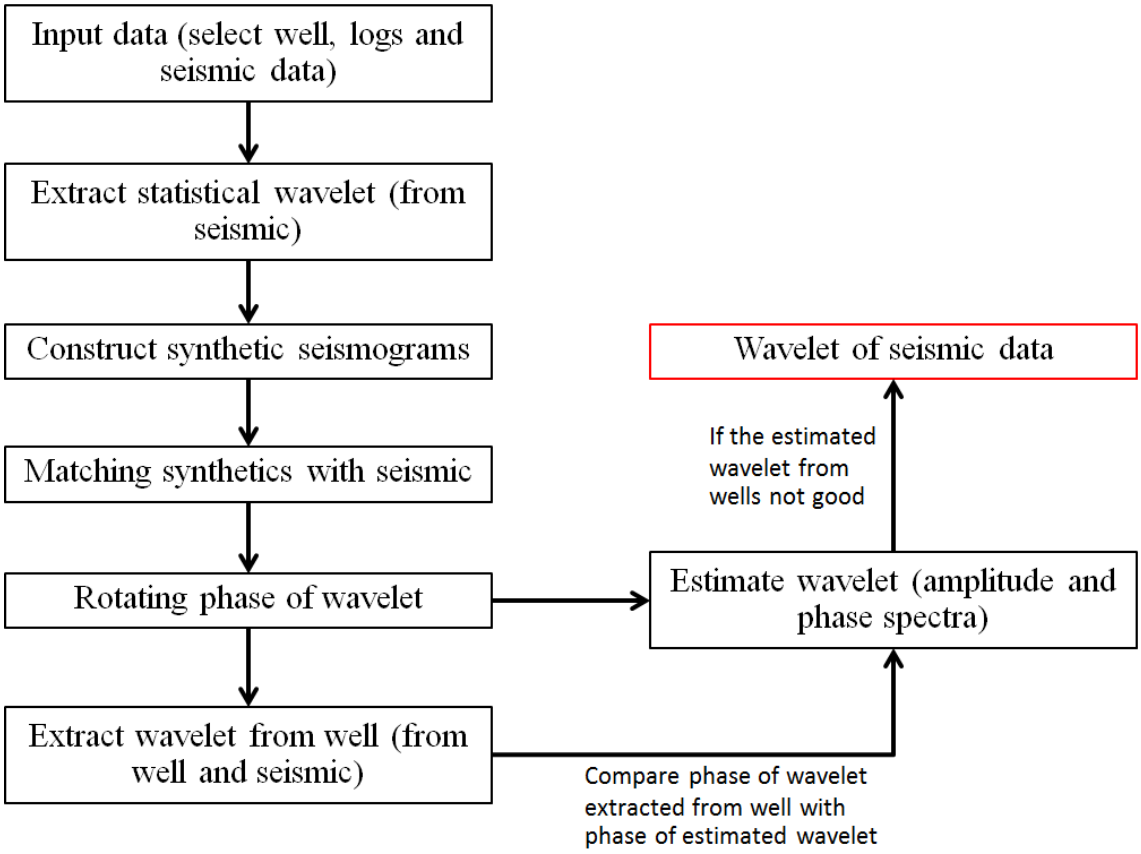

Figure 5.3: Procedure of wavelet estimation.

In the Well A, the wavelets are extracted using Fourier transform of seismic traces located near the well. The statistical wavelets are extracted from 2500 ms to 3200 ms where is zone of interest for full stack, near, mid and far angle stacks (Figure 5.4). These statistical wavelets have constant phase assumption, wavelength of 200 ms and taper length of 25ms. In the time domain of the statistical wavelets, the amplitudes of four wavelets are same and equal 1 as the highest amplitude. However, the central lobes of the wavelets become wider from full stack to near, mid and far angle stacks. In the amplitude and phase domain, bandwidth of the wavelet become narrower of 10 - 50 Hz, 11 - 39 Hz, 10 - 37 Hz and 9 - 32 Hz from full stack to near, mid and far angle stacks respectively.

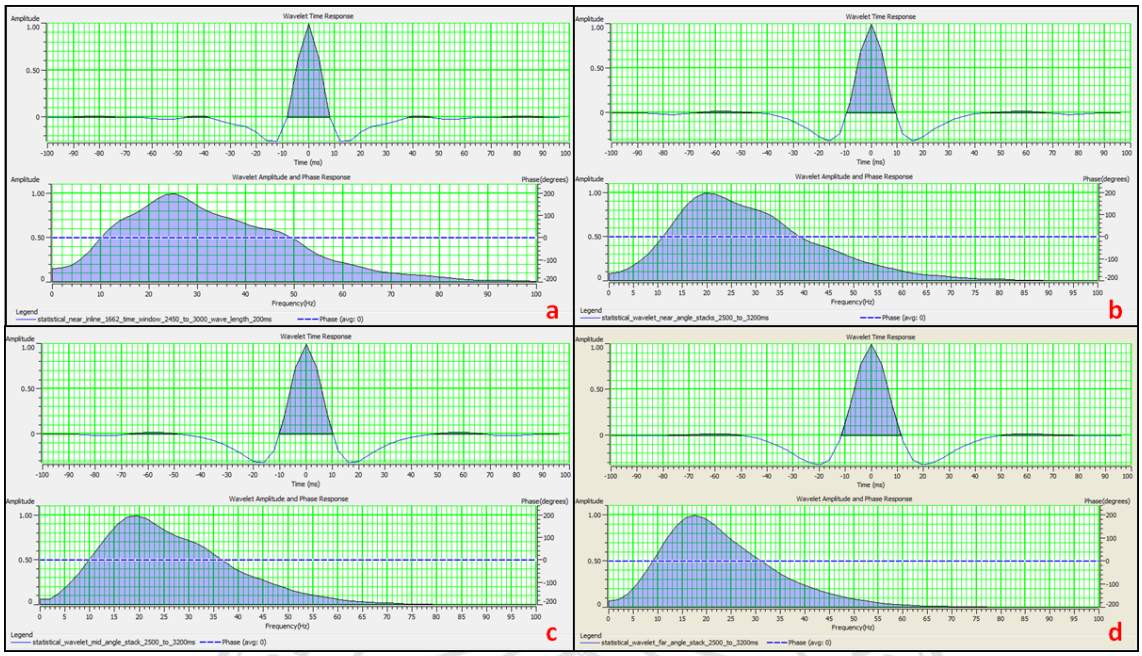

Figure 5.4: Statistical wavelets extracted from seismic data, (a) from full stack, (b) from near angle stack, (c) from mid angle stack, (d) from far angle stack.

To tie the well to the full stack volume using statistical wavelet, a synthetic is generated at the zero offset (normal incident angle) to correlate with one line in seismic data that cross the well location. The line is stacked using traces from 0 m to 500 m in range of offset in order to avoid effects of stretching which caused by NMO correction at the far offset. To tie the well to the near, mid and far angle stacks using statistical wavelet, three synthetics are generated at the incident angles of 6.5 degrees, 19.5 degrees and 33 degrees in near, mid and far angle stacks correspondingly. This synthetics are generated by convolving the reflectivity derived from Vp, Vs and density logs of Well A using the elastic impedance equation (Connoly, 1999) with the zero phase wavelet as shown in Figure 5.4.

Figure 5.5 to 5.8 show how the synthetics tie with full stack, near, mid, and far angle stacks for the Well A respectively. The blue traces are the synthetic while the red traces are the composite traces from seismic data and the black traces are the full stack, near, mid and far angle stacks accordingly. Cross correlation windows between the synthetics and seismic traces are from 2500 ms to 3200 ms that cover two reservoirs UMA15 and MMF30.

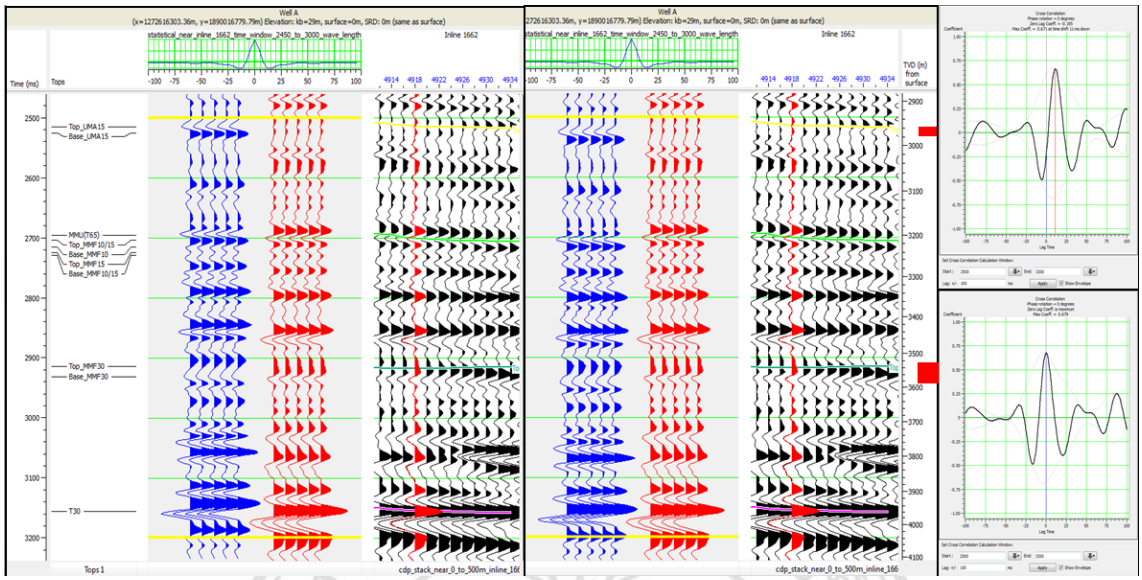

Figure 5.5: Synthetic tie with full stack using statistical wavelet for Well A before and after time shift. The red square indicates the reservoir intervals. The blue traces represent the synthetic while the red traces represent the real seismic data at the well location. The wavelets in the right hand side indicate the cross correlation (CC) between synthetics and real seismic trace. CC increase from -0.195 to 0.679 after time shift of 11 ms down.

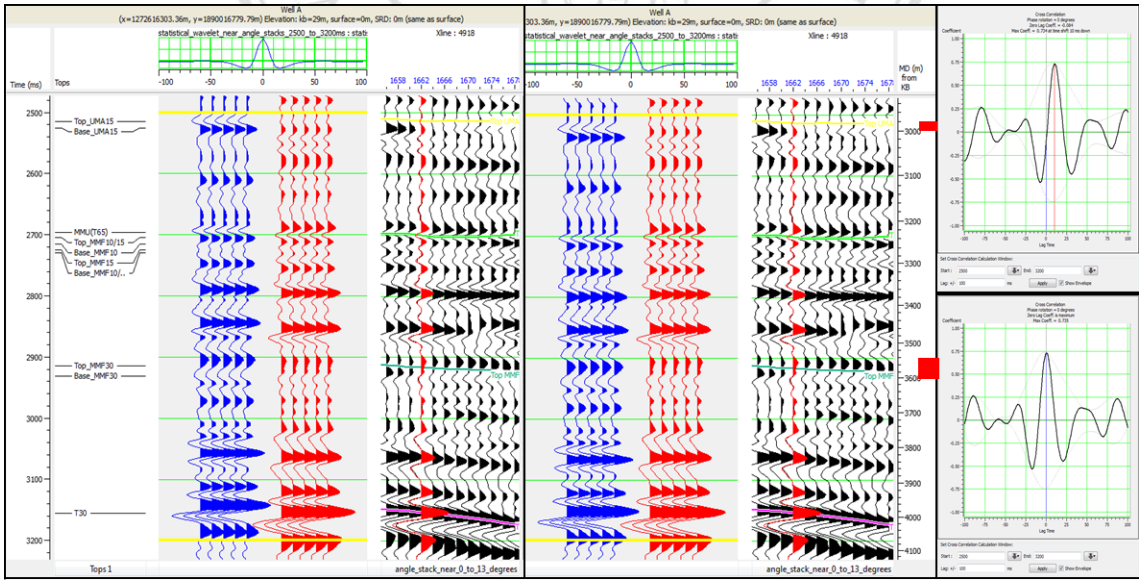

Figure 5.6: Synthetic tie with near stack using statistical wavelet for Well A before and after time shift. The red square indicates the reservoir intervals. The blue traces represent the synthetic while the red traces represent the real seismic data at the well location. The wavelets in the right hand side indicate the cross correlation (CC) between

synthetics and real seismic trace. CC increase from -0.084 to 0.735 after time shift of 10 ms down.

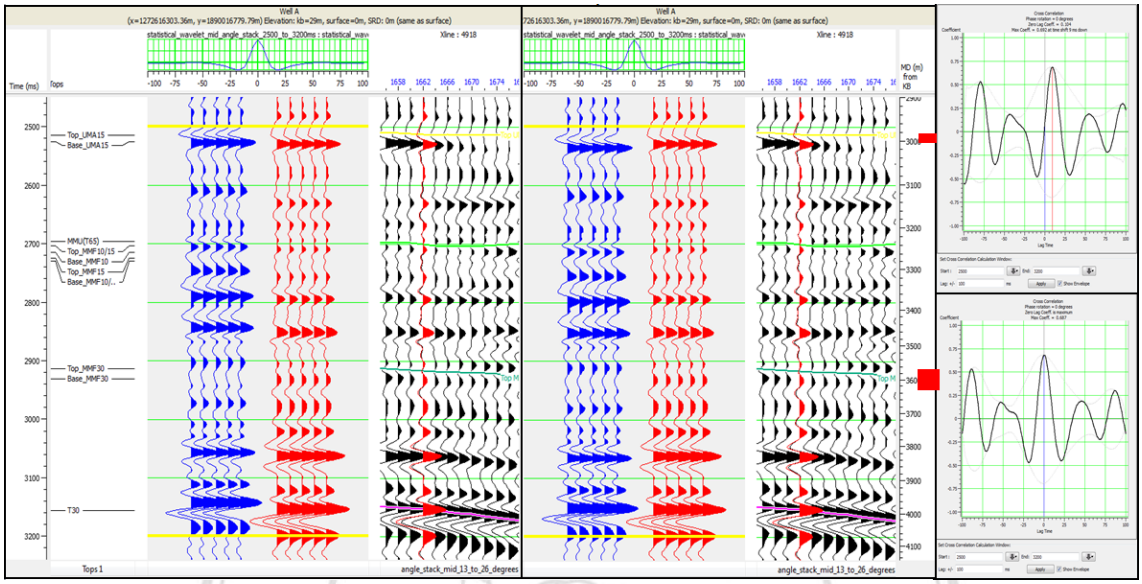

Figure 5.7: Synthetic tie with mid stack using statistical wavelet for Well A before and after time shift. The red square indicates the reservoir intervals. The blue traces represent the synthetic while the red traces represent the real seismic data at the well location. The wavelets in the right hand side indicate the cross correlation (CC) between synthetics and real seismic trace. CC increase from 0.104 to 0.687 after time shift of 9 ms down.

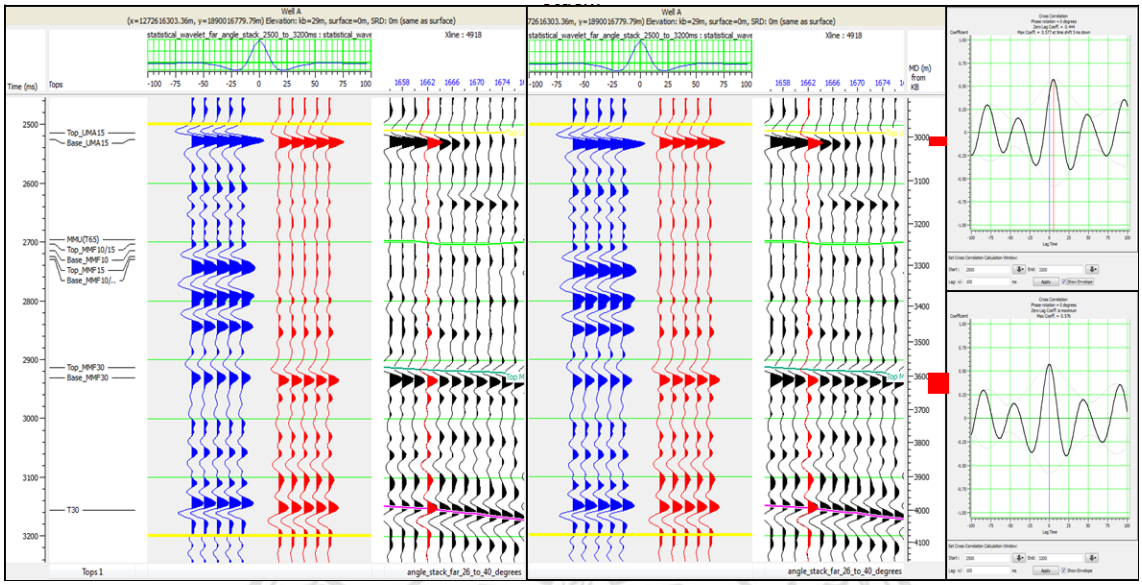

Figure 5.8: Synthetic tie with far stack using statistical wavelet for Well A before and after time shift. The red square indicates the reservoir intervals. The blue traces represent the synthetic while the red traces represent the real seismic data at the well location. The wavelets in the right hand side indicate the cross correlation (CC) between synthetics and real seismic trace. CC increase from 0.444 to 0.576 after time shift of 5 ms down.

As showing in Figure 5.3, the next step is rotating the phase of the wavelets that construct the synthetics to achieve a better cross correlation and especially to get the information about the phase of wavelet in seismic data. In reality, the original phase of the wavelet in seismic data is not zero-phase; therefore in processing, seismic data is often converted to zero-phase to improve resolution and support interpretation. By rotating the phase of the wavelet after assuming zero-phase in correlation process, the real phase of seismic data is then reached with the amplitude spectrum same as the input wavelet. The cross correlation windows show discrepancy between the synthetic traces and the composite traces, it would show symmetric shape when the phase spectrums of the synthetic and the real seismic traces are identical. From Figure 5.5 to Figure 5.8, the cross correlation windows are not symmetrical, so phase rotations are carried out to change the cross correlation window to zero-phase and find the differences in phase between the synthetic and composite traces. Phase rotations of wavelets after well to seismic correlation and the improved cross correlation is shown from Figure 5.9 to Figure 5.12.

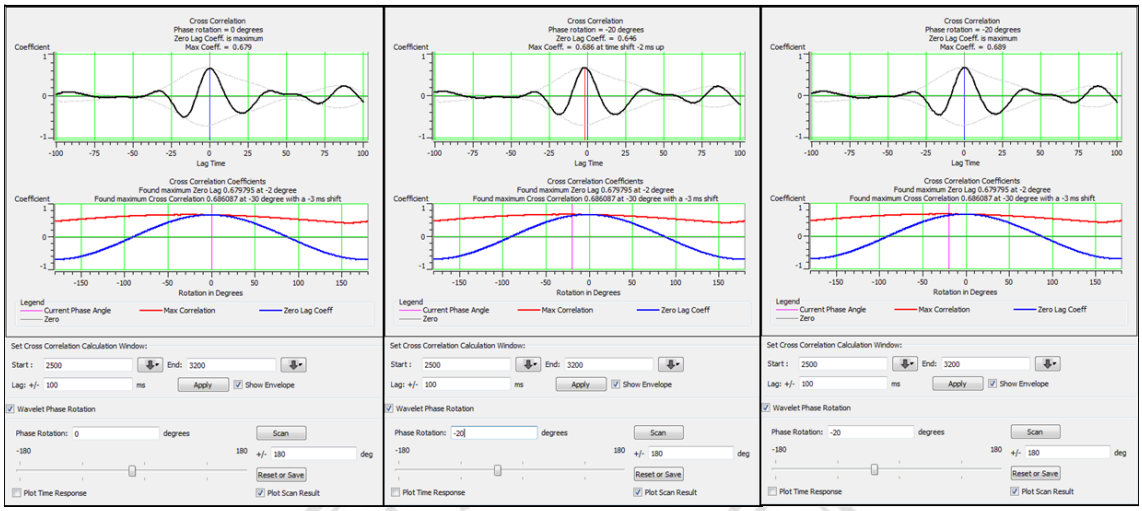

Figure 5.9: Phase rotation of wavelet for well to full stack correlation using statistical wavelet. Cross correlation after phase rotation increases from 0.679 to 0.689. The wavelet phase rotation parameter shows -20 degrees.

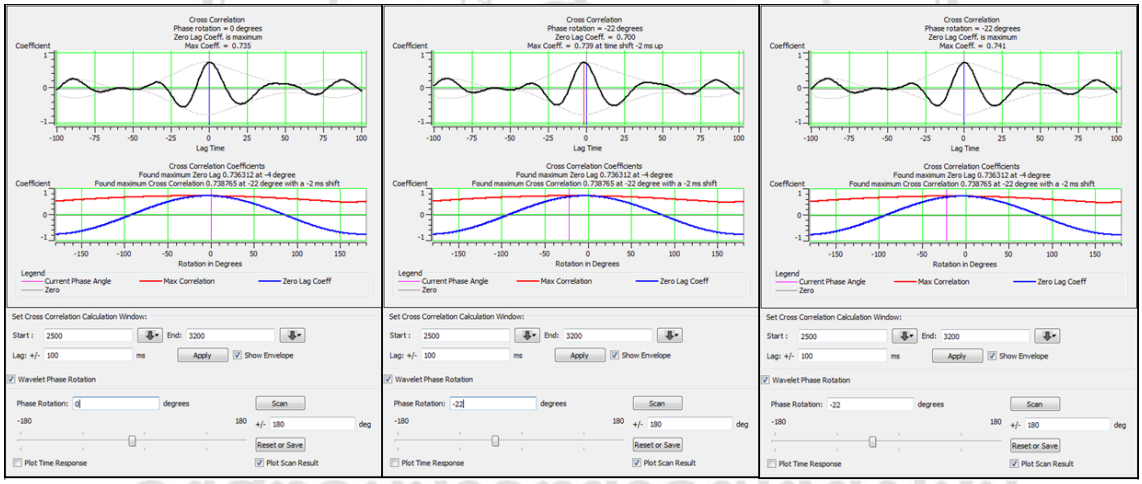

Figure 5.10: Phase rotation of wavelet for well to near angle stack correlation using statistical wavelet. Cross correlation after phase rotation increases from 0.735 to 0.741. The wavelet phase rotation parameter shows -22 degrees.

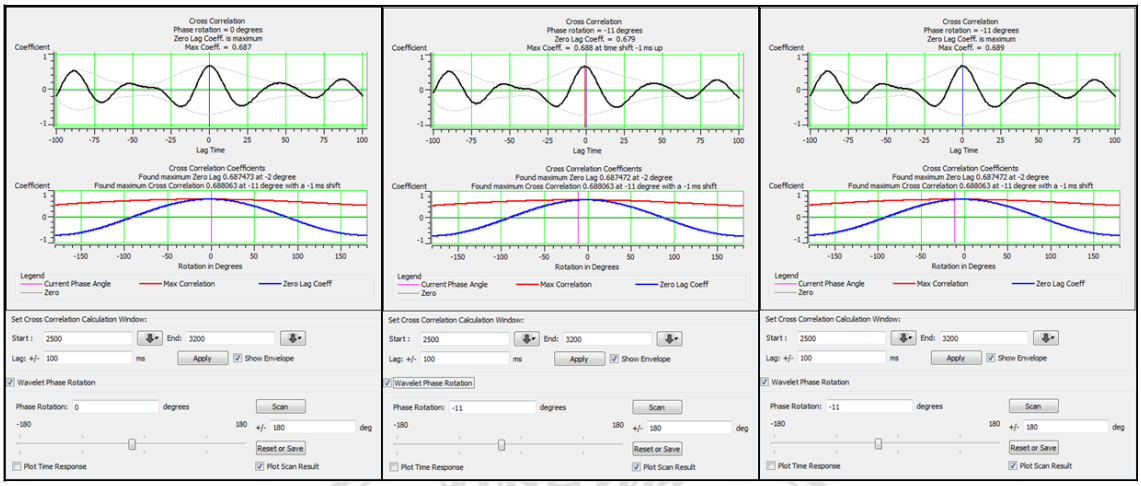

Figure 5.11: Phase rotation of wavelet for well to mid angle stack correlation using statistical wavelet. Cross correlation after phase rotation is increases from 0.687 to 0.689. The wavelet phase rotation parameter shows -11 degrees.

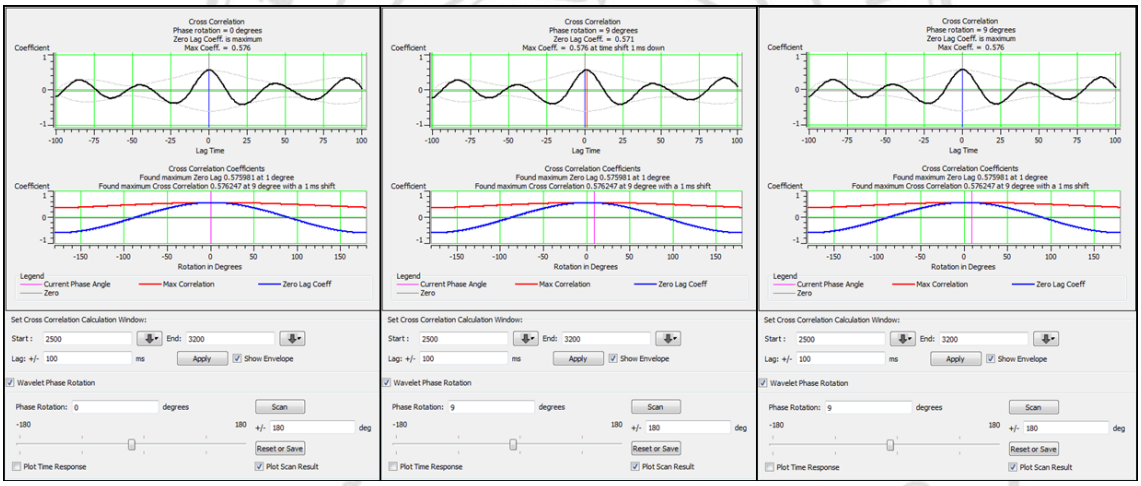

Figure 5.12: Phase rotation of wavelet for well to far angle stack correlation using statistical wavelet. Cross correlation after phase rotation remains constant at 0.576. The wavelet phase rotation parameter shows 9 degrees.

The phase rotation parameters (Figure 5.9 to 5.12) are the phase spectrum information of the seismic data. After wavelet phase rotation the cross correlation windows show symmetric shape at zero time lag. That means the phases of the wavelets which construct the synthetics are identical to the wavelets of seismic data. The estimated wavelets are then extracted with new phase and amplitude spectrum for full stack, near, mid and far angle stacks (Figure 5.13).

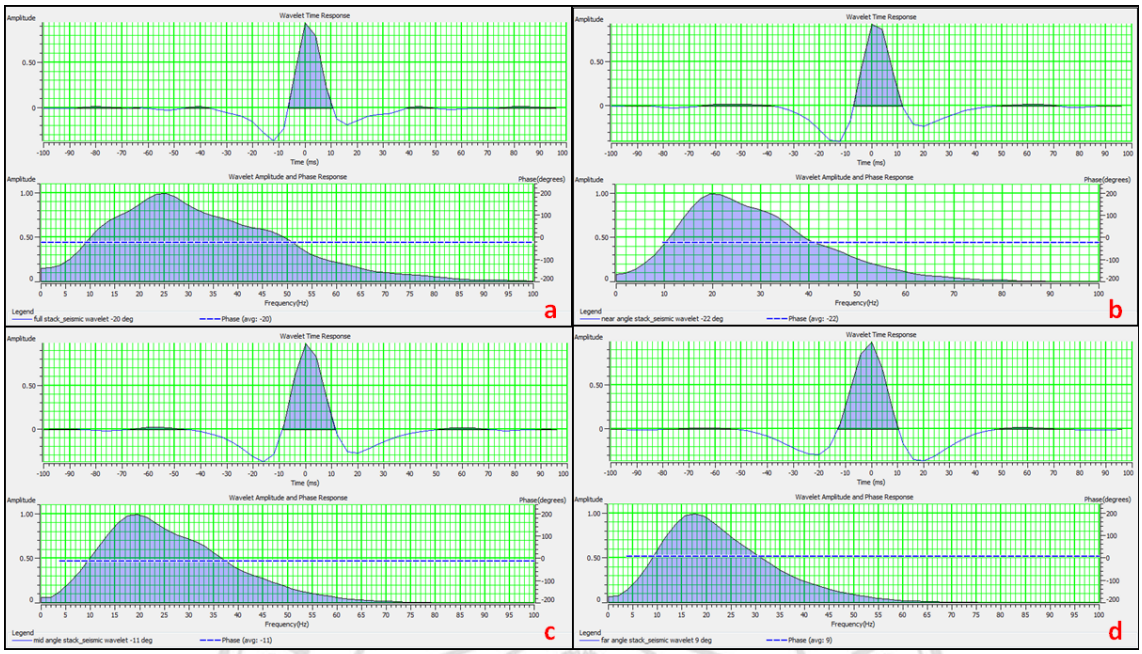

Figure 5.13: Estimated wavelets of seismic data. (a) from well to full stack tie, (b) from well to near angle stack, (c) from well to mid angle stack tie, (d) from well to far angle stack tie.

The second method is extracting the wavelets using wells. Actually this method still use the extracted wavelet from the seismic data around the well location but using the reflectivity from well to determine the phase. Figure 5.14 shows the extracted wavelets from wells. These wavelets have constant phase as extraction type, wavelength of 200 ms, taper length of 25ms and the neighbor trace around the well is 1. In the time domain of the wavelets, the amplitudes of four wavelets are 0.85 at -4 ms time delay, 0.9 at -4 ms time delay, 1 at 0 ms time delay, -0.8 at -8 ms time delay as the highest amplitude for full stack, near, mid and far angle stacks respectively. In the amplitude and phase domain, well and full stack wavelet has phase of 44 and bandwidth of 6 – 31 Hz, well and near angle stack wavelet has phase of 35 and bandwidth of 6 - 30 Hz, well and mid angle stack wavelet has phase of 8 and bandwidth of 6 – 33 Hz, well and far angle stack wavelet has phase of -113 and bandwidth of 5 – 33 Hz.

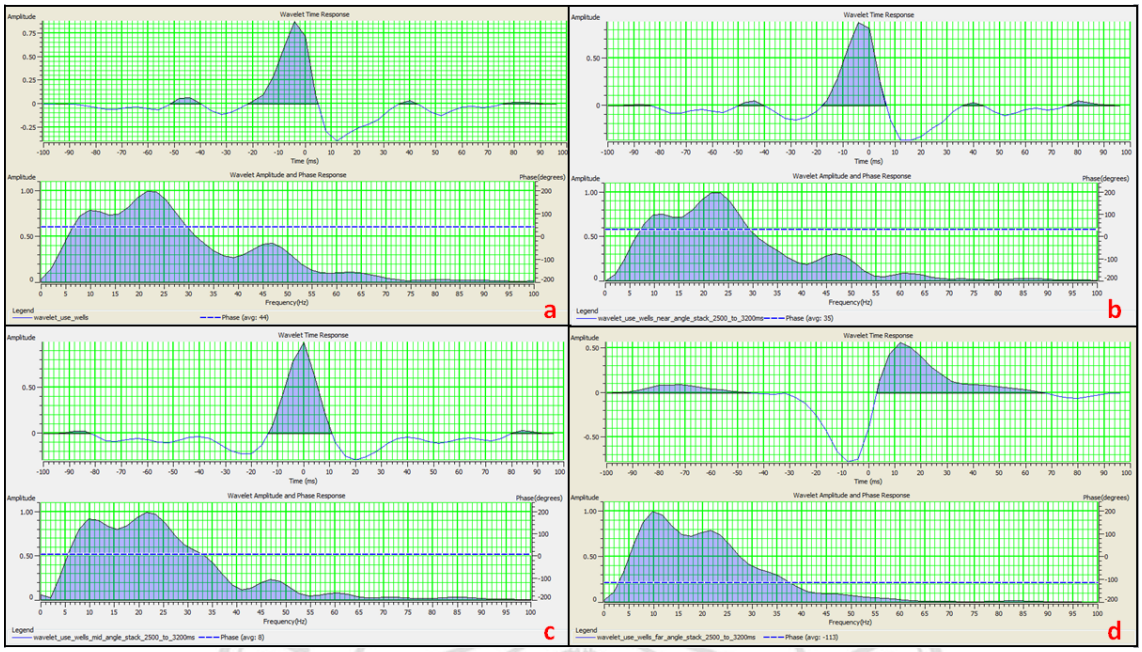

Figure 5.14: Wavelets extracted using well and seismic data. (a) from full stack, (b) from near angle stacks, (c) from mid angle stack, (d) from far angle stack.

Then the phases of extracted wavelets using well would be compared with the phase of estimated wavelet, if the phases of the wavelets are identical between two methods, the phases of extracted wavelets are the phases of wavelets in seismic data. In this case, unfortunately, there are large differences between phases of extracted wavelets using well and phases of estimated wavelets using statistical approach, the phases are list accordingly: -20 degrees and 44 degrees for full stack, -22 degrees and 35 degrees for near angle stack, -11 degrees and 8 degrees for mid angle stack, 9 degrees and -113 degrees for far angle stack. That means the phases of extracted wavelets are not reliable and the wavelets that extracted using phase rotation (Figure 5.13) are used later for AVO modeling and impedance inversion.

5.3 Fluid Replacement Modeling (FRM)

The fluid substitution modeling, which called fluid replacement modeling in Hampson Russell software, plays a vital role in seismic attributes studies because it allows interpreter to see what well logs would look like with different fluid scenarios in the formation, which would cause AVO anomalies in seismic reflectivity. The fluid substitution has discussed by many authors, firstly by Biot (1941) and Gassmann (1951) with their poroelasticity theory, and later such as Baztle and Wang (1992), Smith et al.

(2003), Han and Batzle (2004) etc. The basis concept of fluid substitution is the Biot-Gassmann theory and the equations for Biot-Gassmann modeling were given by Gregory (1977). In this independent study, the available logs are Vp, Vs, density while the porosity and water saturation are estimated as shown in chapter 4 above. All these logs would be used as input data for the fluid replacement modeling. There are two types of equations have been used in the fluid replacement modeling. The first is Gassmann's equation with the formulations from Avseth et al. (2006), it is used to relate the bulk modulus of a rock to its pore, frame and fluid properties and compute the velocities and densities of a set of fluids from the initial set of fluids with corresponding Vp, Vs and ρ. The second is a set of rock physics formulas from Baztle and Wang (1992), it is used to calculate the density and bulk modulus of all in-situ fluids.

Application of Gassmann's equation is based on several assumptions that mentioned by Smith et al. (2003), Wang (2001) and Simm and Bacon (2014). The rock is homogeneous and isotropic, all pores are interconnected, the pores filled with frictionless fluid, wave-induced pressure changes throughout the pore space have time to equilibrate (low frequency assumption) and pore fluid does not interact with the solid to soften or harden the frame.

Figure 5.15 and 5.16 show plots of P-wave velocity, S-wave velocity and Density for UMA15 and MMF30 reservoir intervals respectively. In two reservoir intervals, the red curve represents the recorded log which contains in-situ fluid of gas and water while the blue curve represents the log when the gas in the reservoir is replaced by brine. For UMA15 reservoir, when replacing in-situ gas by brine, there is a significant increase of about 10 % in P-wave velocity and about 8 % in density while the S-wave velocity decrease just 3 %. For MMF30, when replacing in-situ gas by brine, there is a very slight increase of about 4 % in P-wave velocity and a slight increase of about 5 % in density while the S-wave velocity remains nearly constant, the S-wave velocity of in-situ gas and brine are still higher than when the reservoir just contains water. In general, presence of gas in the reservoirs causes much more effects in P-wave velocity and density rather than S-wave velocity.

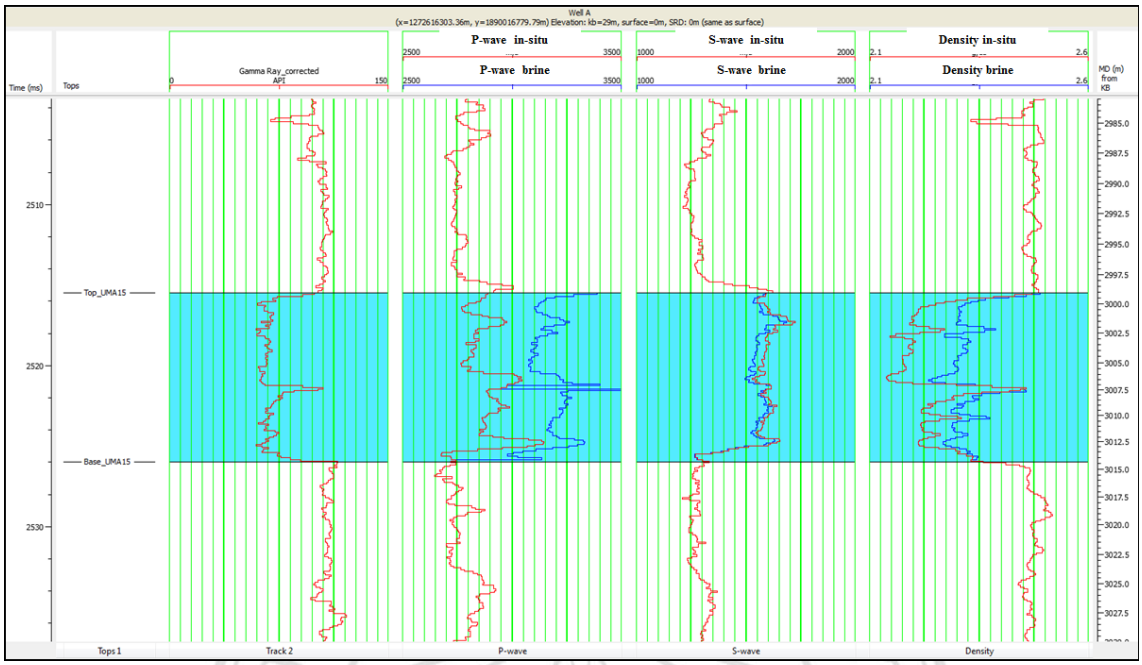

Figure 5.15: In-situ gas (red curve) is replaced by brine (blue curve) for UMA15 in the Well A. (From left to right) Gamma ray, P-wave velocity, S-wave velocity and Density.

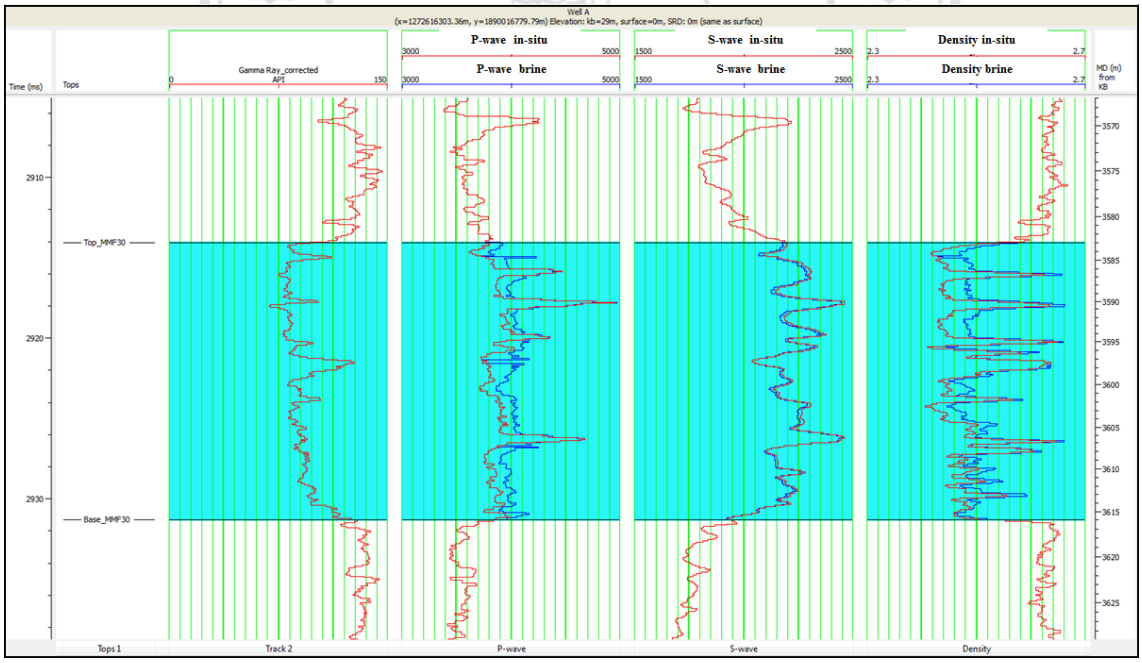

Figure 5.16: In-situ gas (red curve) is replaced by brine (blue curve) for MMF30 in the Well A. (From left to right) Gamma ray, P-wave velocity, S-wave velocity and Density.

5.4 AVO Gradient Analysis

Intercept/gradient analysis is one of the important parts in AVO analysis. In Hampson Russell software, this analysis function is called Gradient Analysis. In this independent study, AVO analysis would not be focused but understanding about the AVO attribute and mapping AVO anomalies would provide essential information about the amplitude variation with offset of reflectivity in seismic data for impedance inversion. The basis equations that used to derive the amplitudes of reflection as a function of angle are Zoeppritz equations. In this study, the amplitudes of the signal for different incident angles are calculated using two terms Aki – Richards approximation, this approximation is refined from Zoeppritz equations by Aki and Richards (1980). Equation 5.1 and 5.2 show the Aki – Richards approximation three terms and two terms respectively:

$$R(\theta) = R_P + Gsin^2\theta + C(tan^2\theta sin^2\theta). \quad (5.1)$$

$$R(\theta) = R_P + Gsin^2\theta, \quad (5.2)$$

where

$R_P = \frac{1}{2}\left(\frac{\Delta V_P}{V_P} + \frac{\Delta\rho}{\rho}\right) = Intercept,$

$G = \frac{1}{2}\frac{\Delta V_P}{V_P} - 4\left(\frac{V_S}{V_P}\right)^2\frac{\Delta V_S}{V_S} - 2\left(\frac{V_S}{V_P}\right)^2\frac{\Delta\rho}{\rho} = Gradient,$

$C = \frac{1}{2}\frac{\Delta V_P}{V_P} = Curvature.$

The result of the Gradient Analysis is the plot of the amplitude of the signal for a reflector against the offset of the trace, in this case is angle that corresponding with the reflector. The plot is intercept and gradient plot, the intercept means amplitude values measurements of reflectivity at zero offset while the gradient means the slope of the curve made by data points. The full angle gathers were used as input seismic for Gradient Analysis. Figure 5.17 and 5.18 show the intercept/gradient analysis for UMA15 and MMF30 reservoirs respectively. It is obvious that there are different AVO anomalies for top and base of two reservoirs. AVO classification is important to understanding polarity (relative hardness), amount of brightening or dimming with offset (relative to the surrounding reflectivity) and whether there is an unusual phase change present with offset (Fogg, 2014). The AVO classes is modified after Rutherford and Williams (1989), Ross and Kinman (1995), Castagna and Swan (1997). Polarity of the seismic data is very important for defining the AVO classes, the polarity of this

seismic data is SEG polarity that has been defined by seabed reflection as positive reflectivity.

The intercept/gradient analysis for UMA15 (Figure 5.17) shows clearly that AVO response at the top of the reservoir (presented by the red event) has very low negative amplitude at normal incident angle, the negative amplitude increase negative value with far incident angle. The AVO response at the base of the reservoir (presented by the green event) has relatively high positive amplitude at normal incident angle, the positive amplitude increase positive value with far incident angle. As expected, the analysis shows a strong class 2 AVO response for the UMA15 reservoir with low negative amplitude intercept and negative amplitude gradient.

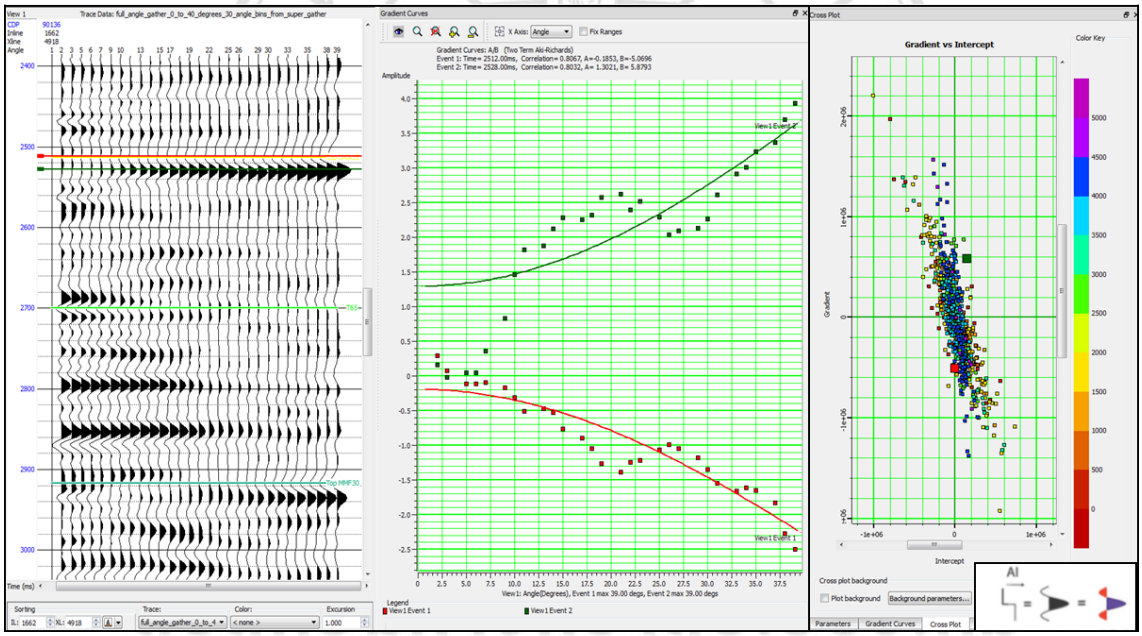

Figure 5.17: Intercept/gradient analysis for UMA15. (from left to right) Full angle gathers seismic data at the Well A location with picked horizons, Intercept/Gradient curves, intercept/gradient cross plot. The red line represents the top of the reservoir while the green line represents the base of the reservoir.

The intercept/gradient analysis for MMF30 (Figure 5.18) shows clearly that AVO response at the top of the reservoir (presented by the red event) has very low positive amplitude at normal incident angle, the positive amplitude decrease to zero ,the phase of reflectivity is reverse and the negative amplitude increase negative value with far incident angle. The AVO response at the base of the reservoir (presented by the green

event) has very low negative amplitude at normal incident angle, the negative amplitude decrease to zero, the phase of reflectivity is reverse and the positive amplitude increase positive value with far incident angle. As expected, the analysis shows a strong class 2P AVO response for the MMF30 reservoir with low positive amplitude intercept and negative amplitude gradient.

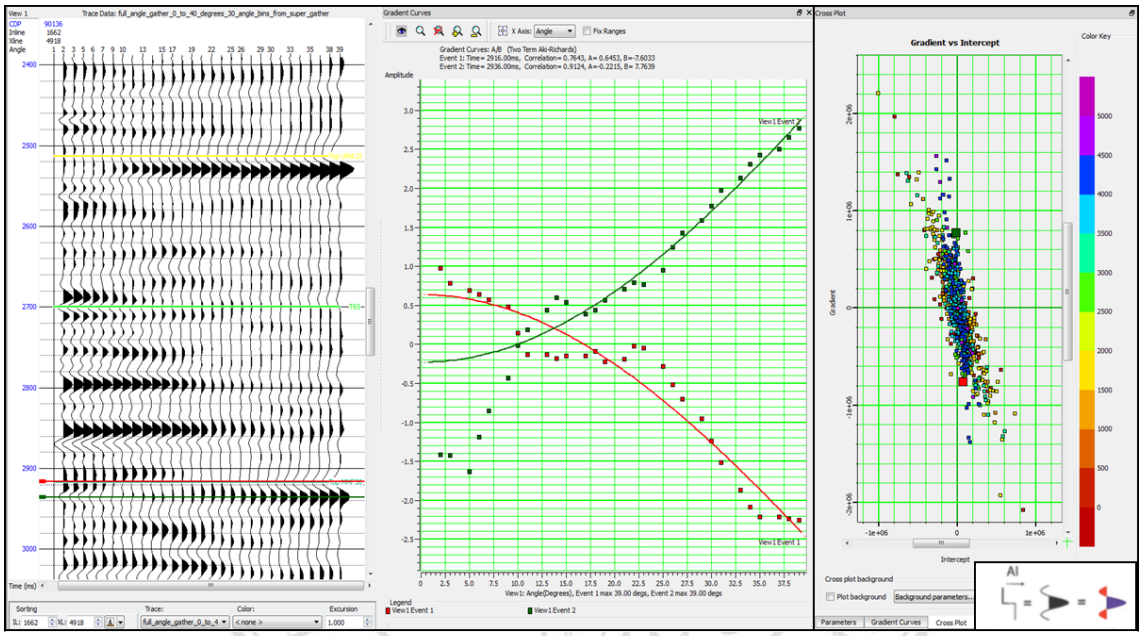

Figure 5.18: Intercept/gradient analysis for MMF30. (from left to right) Full angle gathers seismic data at the Well A location with picked horizons, intercept/gradient curves, intercept/gradient cross plot. The red line represents the top of the reservoir while the green line represents the base of the reservoir.

5.5 AVO Synthetic Models

One of the main objectives in AVO study is to generate a synthetic seismogram and compare with the real seismic dataset in either offset or angle domain. This objective is the key to using AVO for fluid identification (Chiburis et al., 1993). Pre-stack AVO synthetic models are created using Zoeppritz equations. These equations relate the incident plane wave and a plane reflector, therefore, amplitude of the reflection is then calculated. In this independent study, the AVO modeling tool in Hampson Russell software is used to generate AVO synthetic seismograms for the Well A using linear Zoeppritz approximations. The synthetics are created in angle domain with range from normal incident angle 0 degree to far angle of 40 degrees. The wavelet used to generate

AVO synthetics (Figure 5.13 (a)) is estimated after the Well A to full stack seismic tie. Besides, AVO program assume that only the reflected P-wave amplitude is used in calculating AVO synthetics. That means the source is assumed to emit P-wave energy, receivers can detect only P-wave energy and other waves such as multiples or converted waves are not take account of.

AVO synthetics are generated mainly in zone of interest, around two reservoirs intervals. Different of saturation levels are set in the target zones, from top of UMA15 reservoir 2999.1 m to base of UMA15 reservoir 3014.4 m and from top of MMF30 reservoir 3583 m to base of MMF30 reservoir 3616 m. Three synthetic scenarios are set: 100 % brine saturation, in-situ of brine and gas saturation and 100 % gas saturation. The in-situ fluids saturations are defined from saturation log (Sw) that is calculated in chapter 4. These synthetic scenarios are then compared with the actual full angle gather in both logs and gathers. These comparisons are carried out in order to identify the discrepancy between logs of different fluid compositions and the amplitude variations with angle in different fluid replacement conditions. Figure 5.19 and 5.21 show AVO synthetic models for the UMA15 and MMF30 reservoirs in different scenarios respectively while Figure 5.20 and 5.22 show the zoom out of the synthetic models. The logs in red color are original logs (in-situ) from the Well A. Meanwhile the logs in blue color represent logs data of the reservoir that is 100 % water saturation. The logs in black color indicate logs data of the reservoir that is 100 % gas saturation. The acoustic impedance logs (AI) are calculated using the equations:

$$I_P = V_P * \rho, \quad (5.3)$$

where

Ip – P-impedance in (m/s)*(g/cc),

Vp – P-wave in m/s,

ρ – Density in g/cc.

The synthetics are generated at well location (Inline 1662 and Cross line 4918) from near angle (0 degree) to far angle (40 degrees) with increment of 1 degree.

In UMA15 reservoir (Figure 5.19), when there is gas in the reservoir, P-wave velocity and S-wave velocity of scenario 100 % gas and scenario in-situ are quite identical whilst there is a very slight difference in density logs when the red density log is lower

around 5 % than the black one. Although there is the very slight difference in density, it causes almost no difference between red AI log and black AI log, the in-situ AI log (red) has very slightly lower value than the 100 % gas saturation AI log (black). When the reservoir is 100 % water saturation, the P-wave velocity in blue is much lower about 30 % than the red and black P-wave velocity. Similarly, the density in blue is lower of 15 % than the red and black density curves. In contrast, the blue S-wave curve is very slight higher than other S-wave curves. The big difference in P-wave velocity and density when there is 100 % water saturation in the reservoir causes much low acoustic impedance (AI) in the sand reservoir UMA15 sandwiched by high AI shale and this leads to a small trough (nearly zero) in reflectivity at the top of the reservoir and a peak in reflectivity at the base of the reservoir. The amplitude of reflection at the top and base of UMA15 remains stable in the 100 % brine synthetic. However, when there is gas in the reservoir, it causes the low AI in the sand reservoir than the under and above shale, this leads to a trough in top of the reservoir and peak in base of the reservoir. In the 100 % gas and in-situ synthetics, the amplitude variations at the top of the reservoir show increase in negative value (trough) from near to far angle while the amplitude variations at the base of the reservoir show increase in positive value (peak) from near to far angle. When there is 100 % gas saturation in the reservoir, the amplitude of reflection vary less and lower value than when there is in-situ saturation in the reservoir. In conclusion, by comparing the AVO synthetic models of difference scenarios, the AVO synthetic of the in-situ saturation in the reservoir is the most similar with the real seismic angle gather, the amplitude variations with angle represent very clearly AVO class 2 in the UMA15 reservoir. The result is more clearly when we see in the zoom out Figure (Figure 5.20).

In the MMF30 reservoir (Figure 5.21), there is almost no difference in S-wave velocity in all fluid compositions conditions. When there is 100 % water saturation in the reservoir, the P-wave velocity in blue and the density in blue are lower of 10 % than the black and the red and black P-wave velocity. For the density logs, the blue density log shows lower density value of 5% and 10 % than the red and the black density logs respectively. The relative difference in P-wave velocity and density when there is 100 % water saturation in the reservoir causes low acoustic impedance (AI) in the sand reservoir MMF30 sandwiched by high AI shale and this leads to a near zero in reflectivity at the top of the reservoir and a peak in reflectivity at the base of the

reservoir. Note that for MMF30 reservoir, in the P-wave velocity, density and AI curves there are several high velocity, density and AI values intervals due to the presence of many tiny shale layers interbedded with sand reservoir. For the in-situ saturation and 100 % gas saturation AI logs, there is nearly no difference between sand reservoir and surrounding shale, this leads to a relatively small peak at near angle and relatively small trough at far angle in top of the reservoir, a relatively small trough at near angle and relatively small peak at far angle in the base of the reservoir. In the 100 % gas and in-situ synthetics, the amplitude variations at the top of the reservoir show gradual decrease in positive value (peak), reversing phase to trough and gradual increase in negative value (trough) from near to far angle while the amplitude variations at the base of the reservoir show gradual decrease in negative value (trough) to zero, reversing phase and gradual increase in positive value (peak) from near to far angle. When there is 100 % gas saturation in the reservoir, the amplitude of reflection vary less and lower value than when there is in-situ saturation in the reservoir. In conclusion, by comparing the AVO synthetic models of difference scenarios, the AVO synthetic when there is brine and gas (in-situ) in the reservoir is the most similar with the actual seismic angle gather, the amplitude variations with angle represent quite clearly AVO class 2P in the MMF30 reservoir. The result is more clearly when we see in the zoom out Figure (Figure 5.22).

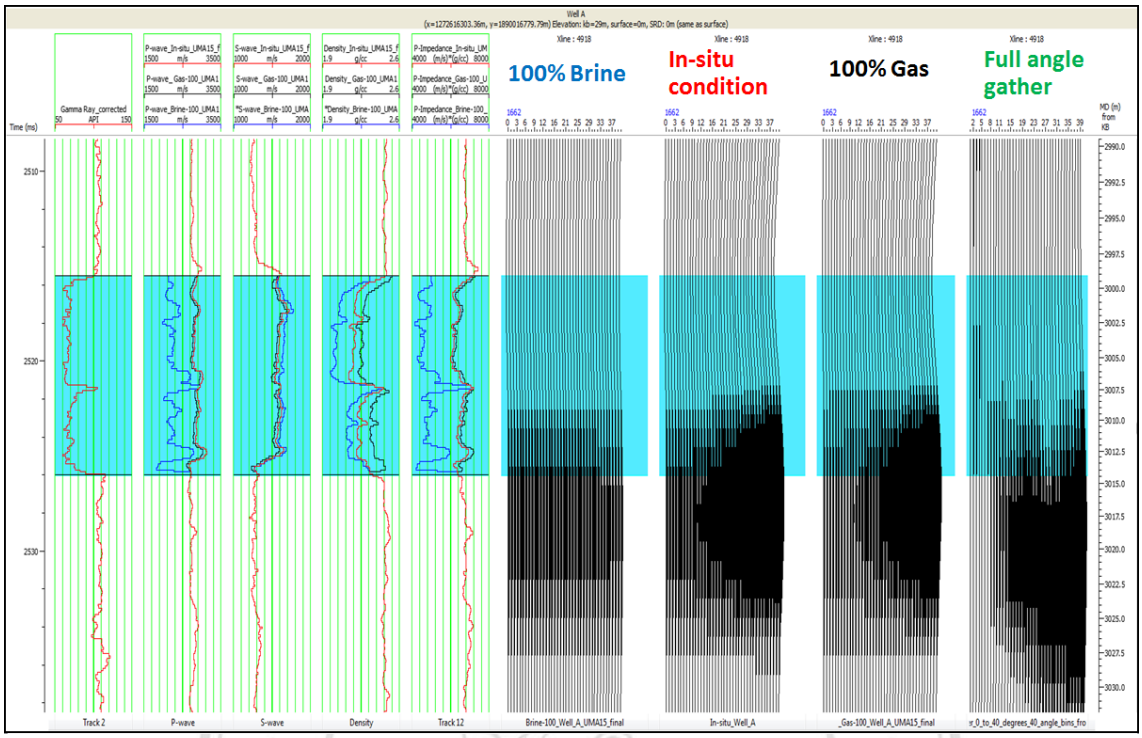

Figure 5.19: AVO synthetic model for the UMA15 reservoir. (from left to right) Gamma Ray, P-wave velocity, S-wave velocity, Density, Acoustic impedance, AVO synthetic of 100%, in-situ, 100% gas and full angle gather.

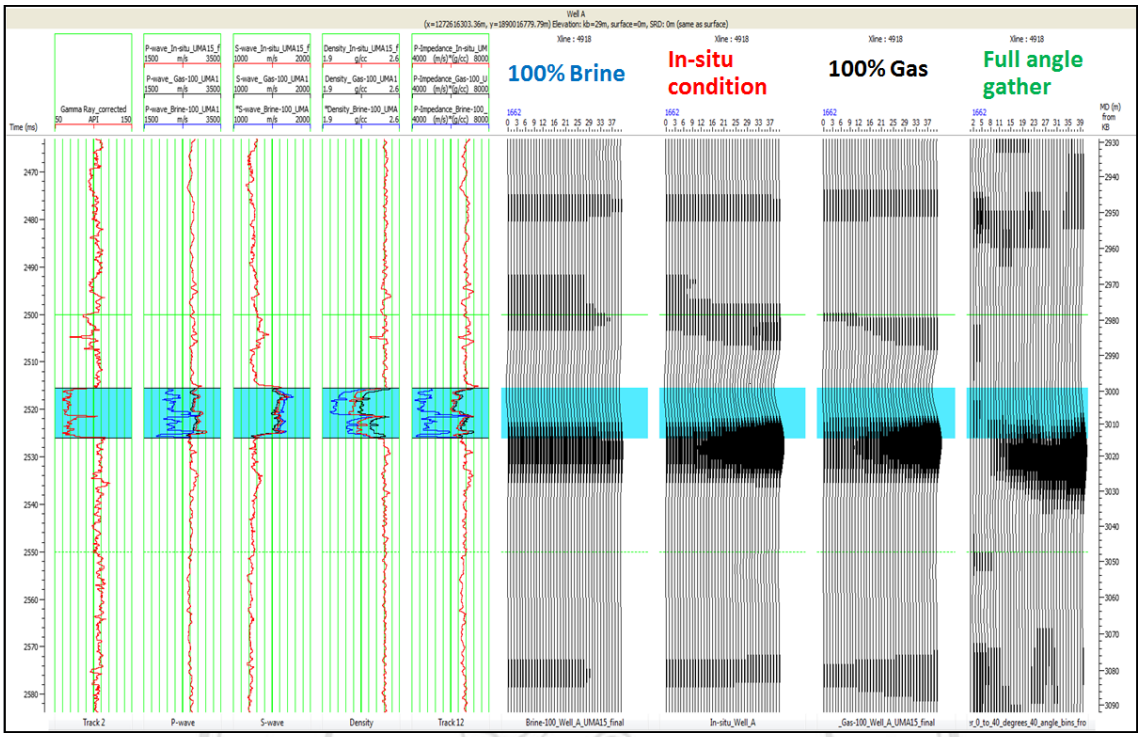

Figure 5.20: Zoom out of AVO synthetic model for the UMA15 reservoir. (from left to right) Gamma Ray, P-wave velocity, S-wave velocity, Density, Acoustic impedance, AVO synthetic of 100% water, in-situ, 100% gas and full angle gather.

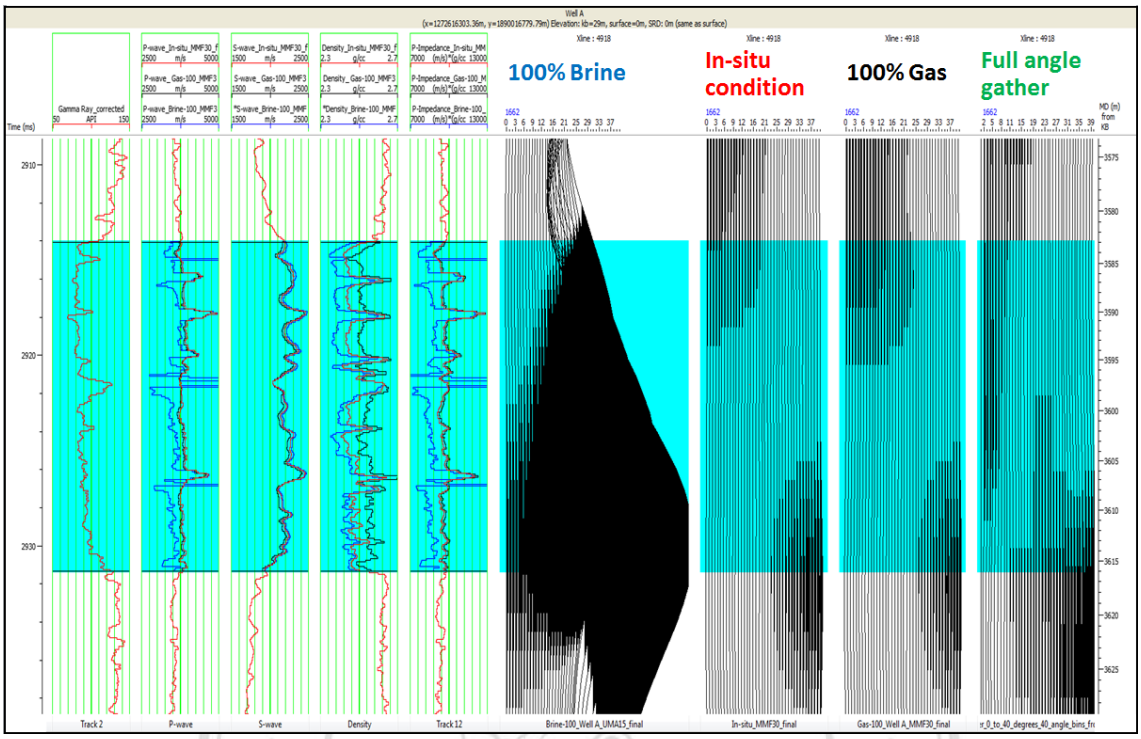

Figure 5.21: AVO synthetic model for the MMF30 reservoir. (from left to right) Gamma Ray, P-wave velocity, S-wave velocity, Density, Acoustic impedance, AVO synthetic of 100% water, in-situ, 100% gas and full angle gather.

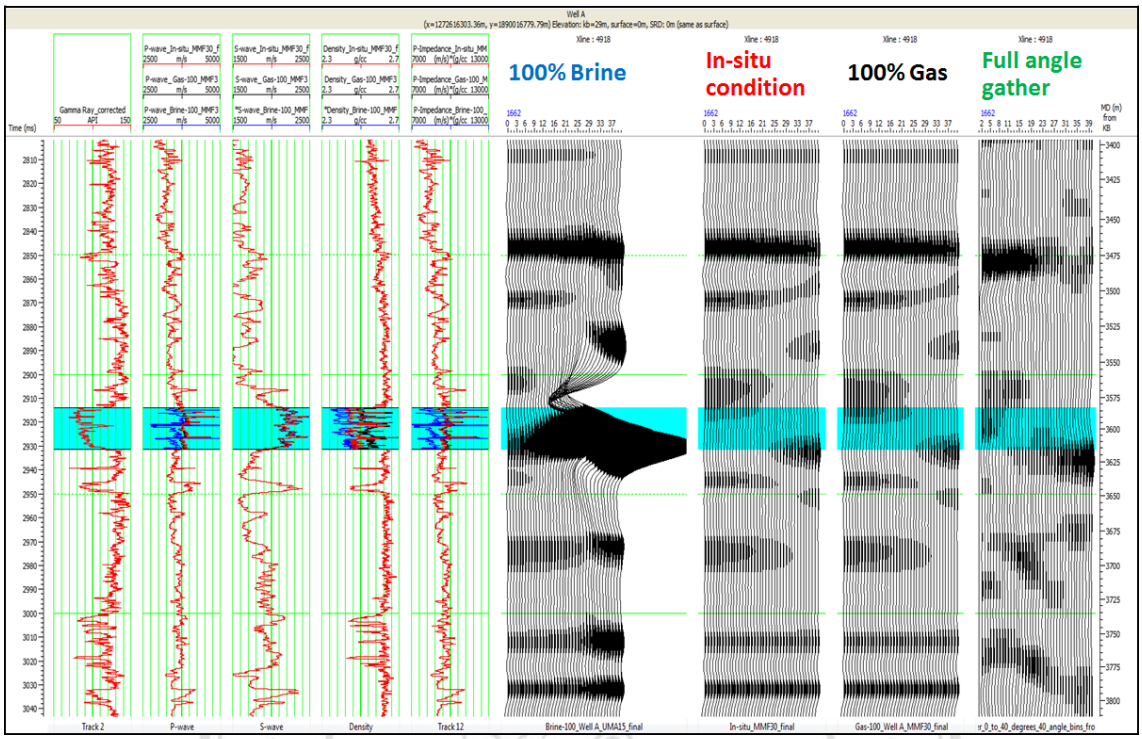

Figure 5.22: Zoom out of AVO synthetic model for the MMF30 reservoir. (from left to right) Gamma Ray, P-wave velocity, S-wave velocity, Density, Acoustic impedance, AVO synthetic of 100% water, in-situ, 100% gas and full angle gather.